

Numerical Simulation of the Formation of Vortices Around Rigid Cylinders as a Issue of Fluid-Structure Interaction Using Immersed Interface Method

As'ad ALIZADEH*, **, Hussein JEBRAIL ZEKRI**, Samad JAFARMADAR***

*Department of Mechanical Engineering, Urmia University of Technology, Urmia, Iran,
E-mail: alizadeh.a.info@gmail.com (Corresponding Author)

**Department of Mechanical Engineering, College of Engineering, University of Zakho, Zakho, Iraq,
E-mail: hussein.zekri@uoz.edu.krd

***Department of Mechanical Engineering, Urmia University, Urmia, Iran, E-mail: S.jafarmadar@Urmia.ac.ir

crossref <http://dx.doi.org/10.5755/j01.mech.26.1.23186>

1. Introduction

From more than one hundred years ago till now days, the flow around objects with circular and square cross sections has attracted the attention of many researchers. The subject of flow around these objects and the phenomenon of vortex shedding caused by that due to practical applications in engineering is of great importance. Among the practical applications of these types of streams, flows around chimneys, high rise buildings, marine structures, suspended bridges, and aircraft's wing, ship's propeller and masts, and many more can be mentioned. This type of flow often involves complex phenomena such as flow separation, vortex flow and vortex shedding. The formation of a vortex behind a rigid fixed cylinder is a complex phenomenon, and despite all theoretical and laboratory studies, there are still many unknown aspects. In this research, we use the immersed interface method to simulate the flow around the rigid cylinders. In this method, the effect of the presence of a body immersed in a fluid by adding a term of force to the Navier-Stokes equations is considered. An important advantage of this method is that there is no compulsion to adapt the points of the fluid mesh and the object mesh. Tatsutani et al. studied voluminous two-dimensional unsteady flow around two square cylinders in a channel with a 20% obstruction ratio in numerical and laboratory methods. They examined the effect of the gap between cylinders on flow behavior in Reynolds numbers between 200 and 1600 [1]. Sohankar et al. [2] examined the fluid flow around the rectangular cylinders at various angles numerically. Their calculations are made for numbers $Re \leq 200$ and angles between zero and 90 degrees. They found that the behavior of all flow parameters at angles of less than 20 degrees and more than 70 degrees had a clear difference with other angles. They [3] also numerically simulated and studied the non-stationary flow around a circular cylinder. His calculations were carried out in the range of numbers $Re = 45-200$. His numerical results showed that for Reynolds, less than 50 flows behind the cylinder are steady and, with increasing Reynolds number, takes on a unsteady state. Patnike et al. [4] simulated the flow of a circular cylinder using finite element method. In the range of numbers $Re = 41-200$, they examined the flow through the effects of buoyancy. Bruno et al. [5] investigated the flow around the cylinder in the Reynolds 40000 by means of a finite volume dissociation method. While Lee and Bienkiewicz [6] applied a finite element method for simulating a

large vortex flow through a square cylinder at 22,000 Reynolds. The advantage of immersed interface method over other computational fluid dynamics methods is that there is no compulsion to adapt the computational grid with the immersed boundaries. So, the flow field can be analyzed numerically using a simple Cartesian mesh domain. In general, the grid points aren't coincided to the immersed intersection. The main idea of this method (Immersed Interface Method) is solving the Navier-Stokes equations over the uniform Cartesian grids. The IIM is introduced by Le Veque and Li [7] to solve the elliptic equations. Then, this method was developed for Stokes flows with the elastic boundaries or surface tension [8]. This method (IIM) was extended to deal with the flexible border problems using the Navier-Stokes equations [9]. The immersed interface method was developed further for the Navier-Stokes equations in [10, 11]. The IIM was also used in [12-14] for solving the two-dimensional stream function vorticity equations on irregular domains. Xu and Wang [15] have extended the IIM to the 3D Navier-Stokes equation for simulating fluid-solid interaction. In this research, using a common immersed interface method, the flow around one and two rigid square cylinders is simulated, and the effects of the blockage ratio and the distance between the cylinders on the formation of vortices are examined.

2. Governing equations

Navier-Stokes equations for the incompressible flow are as follows:

$$\nabla \cdot \vec{u} = 0, \quad (1)$$

$$\rho \left(\frac{\partial \vec{u}}{\partial t} + \vec{u} \cdot \nabla \vec{u} \right) = -\nabla p + \eta \nabla^2 \vec{u} + \vec{F}, \quad (2)$$

with boundary and initial condition [16]:

$$\left. \begin{aligned} u|_{\partial E} &= u_{body} \\ u(x, 0) &= u_{body} \end{aligned} \right\}, \quad (3)$$

where: u is the fluid velocity; p is the pressure; ρ is the density and μ the viscosity of the fluid. The force F which has the form:

$$\bar{F}(\bar{x}, t) = \int_{r(t)} f(s, t) \delta(\bar{x} - \bar{X}(s, t)) ds, \quad (4)$$

where: $\bar{X}(s, t)$ is the arc-length parameterization of $\Gamma(t)$ is the arc-length, $x(x, y)$ is spatial position, and $f(s, t)$ is the force density. Here, $\delta(x)$ is the Dirac function. The motion of the interfaces is shown as below formulation:

$$\bar{u}(\bar{X}(s, t), t) = \frac{\partial \bar{X}(s, t)}{\partial t} = \int_E \bar{u}(x, t) \delta(\bar{x} - \bar{X}(s, t)) d\bar{x}. \quad (5)$$

The force density using an expression of the form:

$$\bar{f}(s, t) = k \left(\bar{X}^e(s) - \bar{X}(s, t) \right), \quad (6)$$

where: k is a constant, $k \gg 1$, and \bar{X}^e is the arc-length parameterization of the required boundary position. The forcing term in Eq. (6) is a particular case of the feedback forcing formulation proposed by Goldstein et al. [17] with $\beta=0$. In [18], the force is expressed as:

$$\bar{f}(s, t) = \alpha \int_0^t \bar{U}(s, t') dt' + \beta \bar{U}(s, t), \quad (7)$$

where: \bar{U} is the velocity at the control points, and α and β are chosen to be negative and large enough so that \bar{U} will stay close to zero.

The Navier–Stokes equations are discretized using a standard finite difference method on a staggered Cartesian grid. Cartesian grid is used for solving interface problems or problems with sophisticated geometry have become popular recently. Existing Cartesian grid methods for interface problems can be classified into two general groups: methods that determine the jump conditions across the interface and include them into the finite difference scheme and our method which is based on the immersed interface method originally proposed by LeVeque and Li [18] falls into the first group. Other methods smooth out the singular force before it is applied to the fluid. When singular forces are applied on a material interface, the solutions of the Navier–Stokes equations may be non-smooth or discontinuous across the interface. Let \bar{n} and $\bar{\tau}$ be the unit outward normal and tangential vectors to the interface, respectively. The respective normal and tangential components of the force density $f_1 = \bar{f}(s, t) \cdot \bar{n}$ and $f_2 = \bar{f}(s, t) \cdot \bar{\tau}$ can be related to the jump conditions for pressure and velocity as follows [13]:

$$[\bar{u}] = 0, [\mu \bar{u}_\xi] = -f_2 \bar{\tau}, [\bar{u}_\tau] = 0, \quad (8)$$

$$[p] = f_1, [p_\xi] = \frac{\partial f_2}{\partial s}, [p_\eta] = \frac{\partial f_1}{\partial s}, \quad (9)$$

$$[\mu \bar{u}_{\xi\xi}] = k f_2 \bar{\tau}, [\mu \bar{u}_{\xi\eta}] = -\frac{\partial f_2}{\partial \eta} \bar{\tau} - k f_2 \bar{n}, \quad (10)$$

$$[\mu \bar{u}_{\xi\xi}] = -[\mu \bar{u}_{\eta\eta}] + [p_\eta] \bar{\tau} - \rho [\bar{u}_\xi] \bar{u} \cdot \bar{n}. \quad (11)$$

The above equations were derived in [13] and here, we have used the same notation for clarity. The jump, $[\cdot]$, denotes the difference between the value of its argument outside and inside the interface, and (ζ, η) are the rectangular coordinates associated with the directions of \bar{n} and $\bar{\tau}$, respectively. Also, k is the signed value of the curvature of the interface. We assume that $\bar{n} \times \bar{\tau} = \bar{k} = \text{constant}$, so that \bar{n} can point either towards, or outwards from, the center of curvature. We note that from above terms the values of the jumps of the first and second derivatives of velocity and pressure taken with respect to the (x, y) coordinates are achieved by a simple coordinate transformation. We consider the below relations as a simple:

$$[\bar{u}_x] = [\bar{u}_\xi] n_1 + [\bar{u}_\eta] \tau_1, \quad (12)$$

$$[\bar{u}_{yy}] = [\bar{u}_{\xi\xi}] n_2^2 + 2[\bar{u}_{\xi\eta}] n_2 \tau_2 + [\bar{u}_{\eta\eta}] \tau_2^2, \quad (13)$$

where: $\bar{n} = (n_1, n_2)$ and $\bar{\tau} = (\tau_1, \tau_2)$ are the Cartesian components of the normal and tangential vectors to the interface at the point considered.

We employ a pressure-increment projection algorithm for the discretization of the Navier–Stokes equations. The velocity field \mathbf{u} and \mathbf{u} are defined at the vertical edges and horizontal edges, respectively. Given the velocity u^n , and the pressure $p^{n-1/2}$, we compute the velocity u^{n+1} and pressure $p^{n+1/2}$, we compute the velocity u^{n+1} and pressure $p^{n+1/2}$ in three steps.

Step 1: compute an intermediate velocity field u^* by solving:

$$\frac{u^* - u^n}{\Delta t} = -(u \cdot \nabla u)^{n+1/2} - \nabla p^{n-1/2} + \mu \nabla^2 u^{n+1/2}. \quad (14)$$

Where, the advective term is extrapolated using the formula:

$$(u \cdot \nabla u)^{n+1/2} = \frac{3}{2} (u \cdot \nabla u)^n - \frac{1}{2} (u \cdot \nabla u)^{n-1}. \quad (15)$$

The diffusion term is approximated implicitly as:

$$\nabla^2 u^{n+1/2} = \frac{1}{2} (\nabla_u^2 u^* + \nabla_u^2 u^n) + C_1. \quad (16)$$

And the pressure gradient term is given by:

$$\nabla^2 u^{n-1/2} = G^{MAC} p^{n-1/2} + C_2. \quad (17)$$

The MAC gradient operators are defined as:

$$(G_x^{MAC} p)_{i+1/2, j} = \frac{p_{i+1} - p_{ij}}{\Delta x};$$

$$(G_y^{MAC} p)_{i, j+1/2} = \frac{p_{ij} + 1 - p_{ij}}{\Delta x}.$$

Step 2: Compute a pressure update Φ^{n+1} by solving the passion equation:

$$\nabla^2 \Phi^{n+1} = \frac{\nabla \cdot u^*}{\Delta t}, n \cdot \nabla \Phi^{n+1} \Big|_{\partial\Omega} = 0. \quad (18)$$

This is accomplished by solving the discrete system:

$$\nabla^2 \Phi^{n+1} = \frac{D^{MAC} u^*}{\Delta t} + C_3. \quad (19)$$

Where the MAC divergence operator is defined as follows:

$$(D^{MAC} u)_{i,j} = \frac{u_{i+\frac{1}{2},j} - u_{i-\frac{1}{2},j}}{\Delta x} + \frac{u_{i,j+\frac{1}{2}} - u_{i,j-\frac{1}{2}}}{\Delta y}.$$

Step 3: Update pressure and velocity field according to:

$$u^{n+1} = u^* - \Delta t G^{MAC} \Phi^{n+1} + C_4, \quad (20)$$

$$p^{n+1/2} = p^{n-1/2} + \Phi^{n+1} - \frac{\mu}{2} (D^{MAC} u^*) + C_5. \quad (21)$$

The operators ∇_h and ∇_h^2 are the standard three point central difference operators and $C_i = 1, \dots, 5$ are the correction terms which are only non-zero at the points near the interface and are calculated using generalized finite difference formulas of the type introduced in the previous section. This method requires solving two Helmholtz equations for u^* in Eq. (14) and ine poisson equation for Φ^{n+1} in Eq. (19).

Having solved fir u^{n+1} at the grid points, we now compute the velocity at the interface. The velocity at the control points, U_k is interpolated from the velocity at the grid points. Thus, we can write:

$$U_k = U(X^k) = B(u^{n+1}), \quad (22)$$

where: B is the bilinear interpolation operator which includes the appropriate correction terms which are required to guarantee second order accuracy when the derivatives of the velocity are discontinuous.

In summary, the equations that need to be solved in order to calculate u^{n+1} and U_k . can be written symbolically as:

$$\text{Eq. (14)} \rightarrow Hu^* = C + B_1 f.$$

$$\text{Eq. (19)} \rightarrow L\Phi^{n+1} = Du^* + B_2 f.$$

$$\text{Eq. (20)} \rightarrow u^{n+1} + u^* - G\Phi^{n+1} + B_3 f.$$

$$\text{Eq. (22)} \rightarrow U_k = Mu^{n+1} + B_4 f.$$

Eliminating u^*, Φ^{n+1}, u^{n+1} from the above equations, we can compute the velocity U_k at the control points as follow:

$$U_k = M(H^{-1}C - GL^{-1}DH^{-1}C) + (M(H^{-1}B_1 - GH^{-1}B_1 - GL^{-1}B_2 + B_3) + B_4) f.$$

For convenience, we can write the above equation as:

$$U_k = U_k^o + Af, \quad (23)$$

where: U_k^o is simply the velocity at the control points obtained by solving Eqs. (14) – (22) with $f=0$, given u^n and $p^{n-1/2}$. A is a $2N_b \times 2N_b$ matrix, where N_b is the number of control points. The vector Af is the velocity at the control points obtained by solving the following equations:

$$\frac{u_f^*}{\Delta f} = \frac{\mu}{2} \nabla^2 u_f^*, u_f^* \Big|_{\partial\Omega} = 0, \quad (24)$$

$$\nabla^2 \Phi_f^{n+1} = \frac{\nabla \cdot u_f^*}{\Delta t}, n \cdot \Phi_f^{n+1} \Big|_{\partial\Omega} = 0, \quad (25)$$

$$u_f^{n+1} = u_f^* - \Delta f \nabla \Phi_f^{n+1}, \quad (26)$$

$$Af = B(u_f^{n+1}). \quad (27)$$

With f being the singular force at the immersed boundary. Eq (23) can be used to determine the singular force if we know the prescribed velocity U_p at the immersed boundary thus, the singular force at the control points can be computed by solving:

$$Af = U_p - U_k^o. \quad (28)$$

The matrix A is computed once and stored. We solve Eqs. (24) – (27) $2N_b$ times, I, e one for each column. Each time, the force strength f is set to zero except for the entry in the column we want to calculate which is set to one. Once the matrix A has been calculated, only the right hand side $U_p - U_k^o$. Needs to be computed at each timestep. The resulting small system of Eq. (28) is then solved at each timestep for the singular force f . Finally, we solve Eqs. (14) – (21) to obtain $u^{n+1}, p^{n+1/2}$.

3. Results and discussion

3.1. Flow analysis around one square cylinders

The problem geometry in this case is shown in Fig. 1, the path blocking ratio is equal to $B=1/8=0.125$ ($B = d / H$). The channel length to obstacle. length ratio is 25. ($L / d = 25$). All dimensions of the cylinders are dimensionless by the length of the square obstacle. The length of the flow input (the distance between the front edge of the square cylinder and the channel entrance) is $L / 5$. The velocity profile is uniform at the entrance and the boundary condition is non-slip on the walls. The Reynolds number is $Re < 300$.

Fig. 2 shows the flow lines for several different Reynolds numbers. Fig. 2, a shows the stream lines in $Re = 1$. In this case, due to the predominance of Viscose forces, a steady flow will be formed without any separation.

As the Reynolds number increases, separation of the flow occurs in the back of the barrier. The onset of the separation phenomenon and the formation of stationary vortices for the present problem is $Re = 3$ (Fig. 2, b). Zdravkovich [19] In his empirical observation, provided this value for a circular cylinder in the free flow with $Re = 4.4$. As can be seen, this value is for a square barrier smaller than the corresponding value for the flow around the circular cylinder. The reason for the smaller value of this value in the flow around the square barrier can be related to the existence of sharp edges in this problem. When the Reynolds number of the upstream flow reaches the critical Reynolds number, alternating unsteady vortex phenomenon occurs. The critical Reynolds number for the studied issue is calculated with blockage ratio of 0.125, about 55. To illustrate this, the stream lines are compared for $Re = 50$ and $Re = 60$ in Figs. 2, c and 2, d. References [20, 21] have provided 54 and 70 respectively for critical values of Reynolds. Fig. 2, e shows the stream lines for $Re = 200$. Since the flow in this case is unsteady, the shape of the stream lines is drawn in a special moment. Flow in $Re = 200$ In addition to the vortex flow behind the cylinder, smaller vortex flows will be formed adjacent to the lateral edges of the cylinder. In other words, the separation region from the back of the cylinder penetrates to the front

edge. Based on the results of the calculations, the penetration phenomenon of the separation region to the front edge can be seen in the Reynolds range greater than 130. This phenomenon has significant effects on the flow characteristics that will be addressed in the following sections.

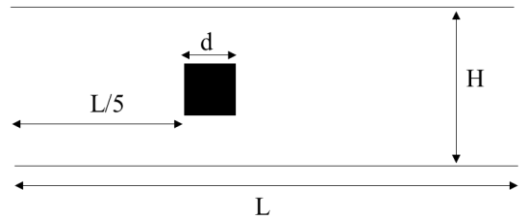


Fig. 1 Problem geometry of a square cylinder

Fig. 3, a shows the variation in vortex region length (steady flow with symmetric vortices) versus Reynolds number. The calculations confirm the linear increase in vortex region length in terms of Reynolds number increase. Fig. 3 shows the variation in the Drag coefficient in terms of Reynolds number in the Reynolds range below 55. In this figure, the results of the calculations are compared with the results of Breuer et al. [22]. In the lower Reynolds numbers, in the calculation of the drag force, the contribution of frictional forces to pressure forces is greater.

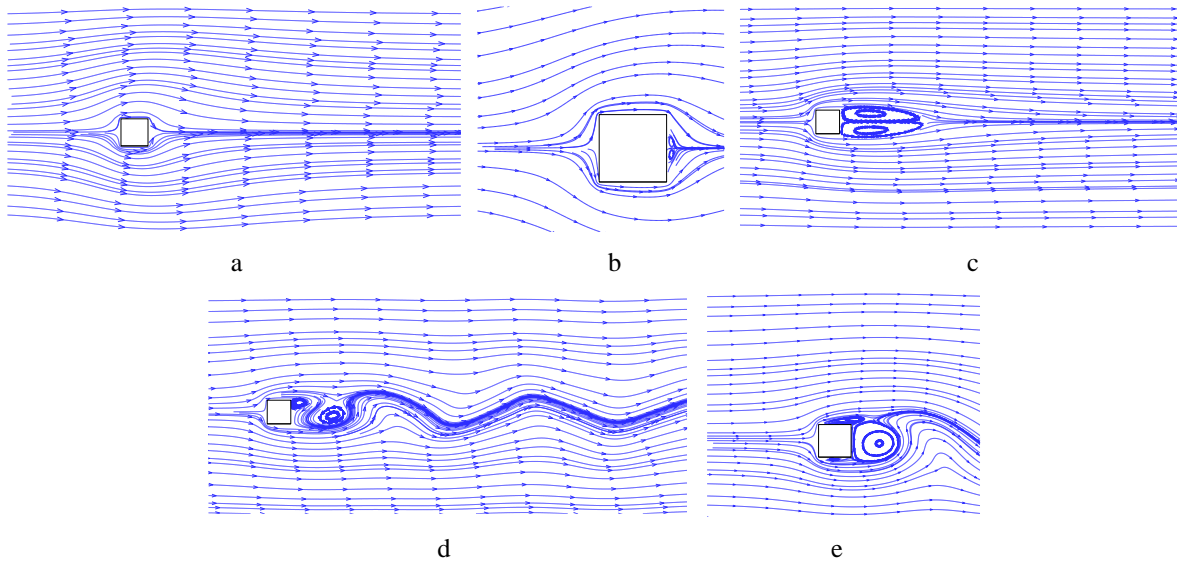


Fig. 2 The stream lines for a - $Re = 1$, b - $Re = 3$, c - $Re = 50$, d - $Re = 60$ and e - $Re = 200$

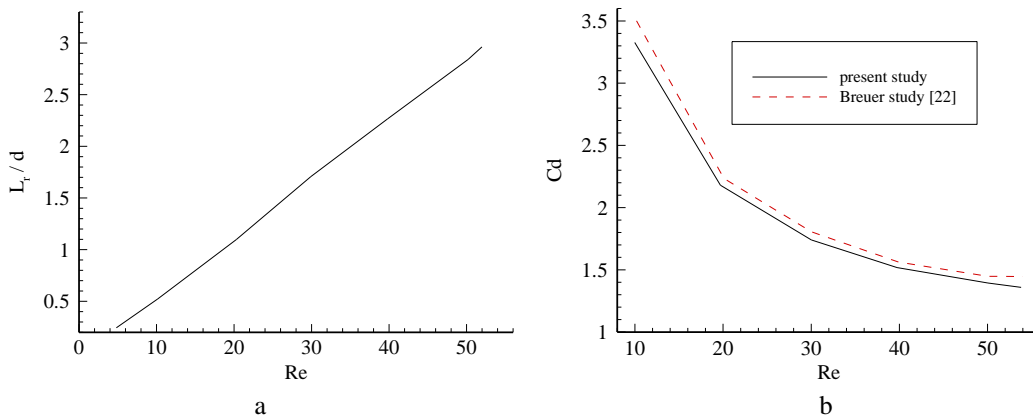


Fig. 3 a - The vortex region length versus the Reynolds number in the permanent flow, b - The variation of the drag coefficient in terms of Reynolds number in the steady flow

Fig. 4 shows the variation of the Strouhal number versus Reynolds number. The results are in good agreement

with the results of Breuer et al. [22]. In the range of $55 < Re < 140$, with the increase of the Reynolds number, the number of strouhal also increases. When the Reynolds number reaches about 140, the graph will have a maximum point, and after that, the Strouhal number begins to decrease gradually. the reason for that is an important change that occurs in the flow pattern as shown in Fig. 2, e. In the Reynolds range greater than 130, the flow separation point moves from the rear edge of the cylinder to the front edge and therefore vortex flows are formed with a smaller scale adjacent to the lateral edges. The occurrence of this phenomenon causes the fluctuating behavior of downstream flow to slow down.

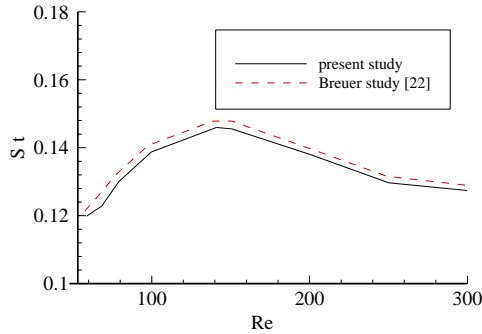


Fig. 4 Strouhal number changes versus Reynolds number

In Fig. 5, the drag coefficient chart in the Reynolds range of less than 130 has a decreasing trend, which is related to the effects of the getting thin of boundary layer. The chart has a minimum point at Reynolds Point 130, and in larger Reynolds, the Drag coefficient increases. This is due to the penetration of the point of separation of the flow from the rear edge of the cylinder towards the front edge, resulting in an appreciable increase in the contribution of the pressure drag force in calculating the drag coefficient. As noted above, the penetration of the separation region to the front edge in the Reynolds range greater than 130 has significant effects on the unsteady flow characteristics and plays a major role in interpreting the changes chart in the Strouhal number and Drag coefficients.

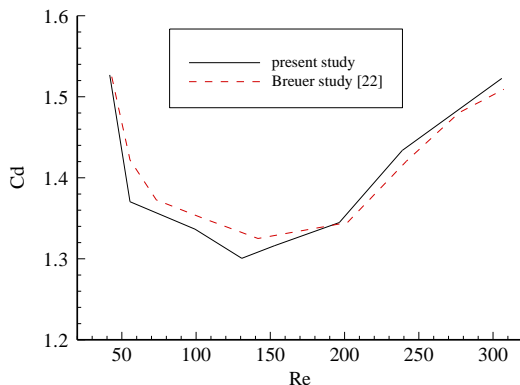


Fig. 5 Changes of the average drag coefficient versus Reynolds number in the unsteady flow

3.2. Flow analysis around two square cylinders

The purpose of this section is numerical study of passing flow from two consecutive cylinders in order to find the effects of the change of Reynolds number, the ratio of blockage and the distance between the barriers on the flow

characteristics. Boundary conditions and channel geometry are similar to the previous problem. The Reynolds number varies between 1 and 200. First, $G = 5$ is considered constant.

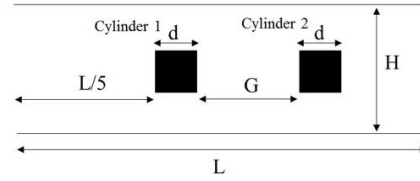


Fig. 6 The geometry of two square-cylinder problem

Fig. 7 shows variations in the coefficient of cylinder drag in the different blockage rates versus the increase in Reynolds number ($G = 5$). Reducing the blockage ratio reduces the drag coefficient and pressing drag coefficient. This is due to the reduction of the effective flow velocity around the cylinders and the strengthening of the pressure in the rotating area behind the cylinders. Increased pressure in the area wake cylinder reduces the pressing drag coefficient and since the large part of the drag coefficient of the cylinders is due to the pressing drag coefficient, the total drag coefficient decreases. With increasing Reynolds, the cylinder drag coefficient 1 (upstream) decreases and the cylinder drag coefficient 2 (downstream) increases. However, by increasing Reynolds, there is a fluctuation in the drag coefficient of 2 that reduces the drag coefficient.

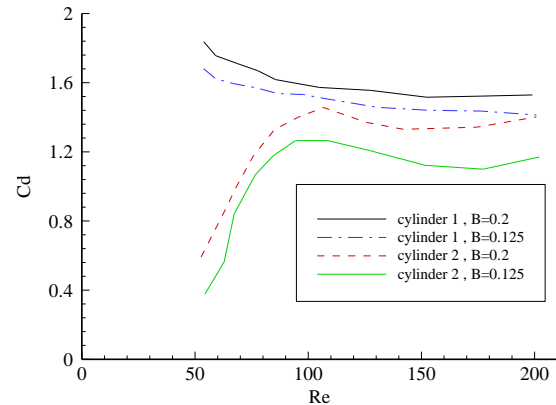


Fig. 7 Changes in cylinder drag coefficient in the different obstruction rates versus increasing the Reynolds number

For the distance between the cylinders $G = 5$, in the Reynolds number range less than 55, flow remain steady, while in the Reynolds number range greater than 55, unsteady flow (periodic) are formed. The critical Reynolds number indicates the beginning of the vortex shedding from both cylinders, for the gap between the cylinder $G = 5$ in the $Re = 55-60$ range. In Fig. 8, the stream lines for $Re = 100$ and the various cylindrical distances $G = 1-5$ are shown. For cylinder spacing $G = 1$, the flow around the cylinder upstream (cylinder 1) and the between two cylinders' area is steady and the vortex shedding occurs only from the downstream cylinder (cylinder 2). As the distance between the two cylinders increases, the flow symmetry in the between two cylinders area fades out and the vortex shedding from both cylinders starts. For the Reynolds number 100, the gap the critical cylinder, which vortex shedding starts from cylinder 1, lies within the range of $G = 1-2$. Reducing the gap

between cylinders will increase the critical Reynolds number. For example, for a gap between cylinders $G = 2$, the critical Reynolds number is within $Re < 100$, while for the cylindrical gap $G = 1$, the critical Reynolds is within the $Re > 100$ range. The critical Reynolds number is a Reynolds, in which the phenomenon of asymmetric vortices shedding

(Von Karman vortex street) starts from both cylinders. Critical Reynolds number can be an important parameter in the design of structures. In such a way that the structural designer can predict the initiation of the vortex's diffusion and actually the application of oscillatory forces on the structure.

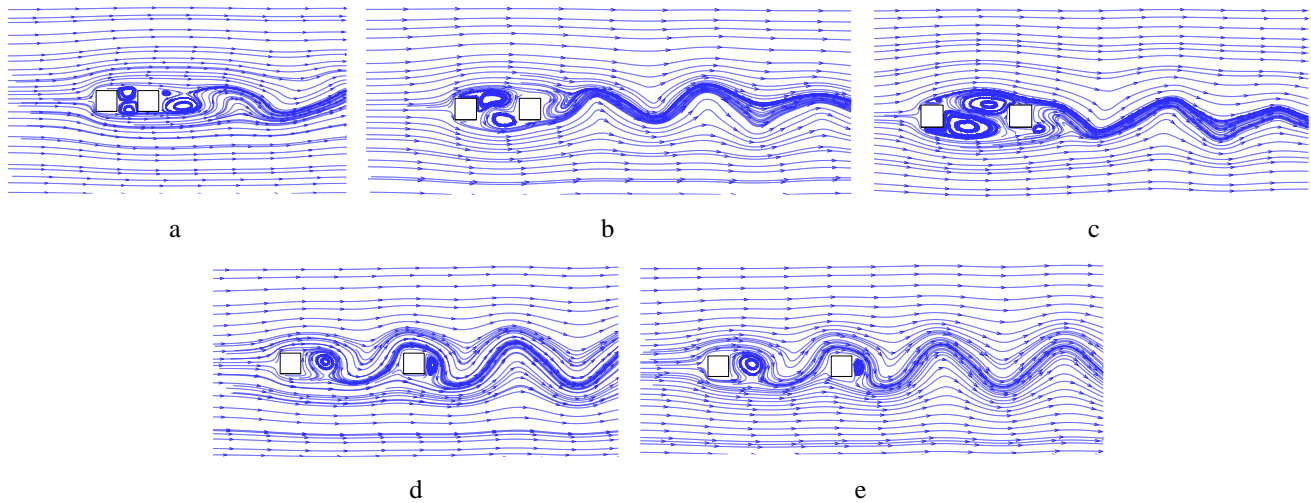


Fig. 8 The stream lines for $Re = 100$: a - $G = 1$, b - $G = 2$, c - $G = 3$, d - $G = 4$ and e - $G = 5$

4. Conclusions

In this research, the immersed interface method is used which is a non-conforming method to the boundary. Eulerian mesh is used for fluid field, and Lagrangian mesh for solid field. The connection between these two mesh is established by the Dirac Delta function. Considering the cylinder as a rigid immersed boundary within the flow. First, simulation laminar flow around a square cylinder has been investigated. 1. In Reynolds less than 1, there is a steady creepage flow and no flow separation occurs. 2. In the Reynolds larger than 3, the separation of the flow occurs and the steady flow is observed with symmetrical and stationary vortices behind the cylinder. 3. In the Reynolds larger than 55 (critical Reynolds), the phenomenon of alternating discharge of vortices (Von Karman shedding Street) and unsteady behavior of flow are observed. 4. In the Reynolds larger than 130, the vortex flow from the back of the cylinder penetrates to the front edge. The results of the calculations show that in the steady flow pattern with symmetric and stationary vortices behind the cylinders in the range $3 < Re < 55$, with the increase of the Reynolds number, the length of the vortex region increases linearly. As the Reynolds number increases, the process of changing the Strouhal number in the range below 140, incremental and in the Reynolds range between 140 and 300 is reduced. Also, with the Reynolds number increasing, the process of changing drag coefficient in the Reynolds range less than 130 declines and within the Reynolds range between 130 and 300 increments. The change in behavior in the process of changing the Strouhal number and the drag coefficient in the range of $130 < Re < 140$ can be related to changing the pattern of flow in this range. The penetration of vortex flow from the back of the cylinder to the front edge is the main cause of this behavior change. In the second part of this study, the flow around the two cylinders has been analyzed. Studies have shown that for $G = 5$, the flow in the Reynolds range less than 55 is steady, while in the Reynolds range greater than

55 unsteady. Passing from steady to unsteady state happens in the $Re = 55-60$ range (critical Reynolds number). Based on the location and flow separation, three different states are observed. 1. Begin separation of the flow from the escape edges of the cylinders in the range $1 < Re < 2$ for the upstream cylinder and $2 < Re < 5$ for the downstream cylinder. 2. Starting the vortex shedding from the edges of the escape of the cylinders in the range of $55 < Re < 60$. 3. Starting separation of the flow from the attack edges of the upstream cylinder in the range of $100 < Re < 125$.

References

1. **Tatsutani, R.; Devarakonda, R.** 1993. Unsteady flow and heat transfer for cylinder pairs in a channel, *International Journal of Heat and Mass Transfer* 36:331-3328. [https://doi.org/10.1016/0017-9310\(93\)90013-V](https://doi.org/10.1016/0017-9310(93)90013-V).
2. **Sohankar, A.; Norberg, C.; Davidson, L.** 1997. Numerical simulation of unsteady flow around rectangular cylinders at incidence, *Journal of Wind Engineering and Industrial Aerodynamics* 69-71:189-201. [https://doi.org/10.1016/S0167-6105\(97\)00154-2](https://doi.org/10.1016/S0167-6105(97)00154-2).
3. **Udaykumar, H. S.; Mittal, R.; Rampunggoon, P.; Khanna, A.** 2001. A sharp interface Cartesian grid method for simulating flows with complex moving boundaries, *Journal of Computational Physics* 174:345-380. <https://doi.org/10.1006/jcph.2001.6916>.
4. **Patnike, B. S.; Narayana, P. A. A.; Seetharamu, K. N.** 2000. Finite element simulation of transient laminar flow past a circular cylinder and two cylinders in tandem influence of buoyancy, *International Journal of Numerical Methods for Heat & Fluid Flow* 10:560-580. <https://doi.org/10.1108/09615530010347169>.
5. **Bruno, L.; Fransos, D.; Coste, N.; Bosco, A.** 2010. 3D flow around a rectangular cylinder: A computational study, *Journal of Wind Engineering and Industrial Aerodynamics* 98:263-276. <https://doi.org/10.1016/j.jweia.2009.10.005>.

6. **Lee, S.; Bienkiewicz, B.** 1998. Finite element implementation of large eddy simulation for separated flows, *Journal of Wind Engineering and Industrial Aerodynamics* 77-78:603-617.
[https://doi.org/10.1016/S0167-6105\(98\)00176-7](https://doi.org/10.1016/S0167-6105(98)00176-7).
7. **LeVeque, R. J.; Li, Z.** 1994. The immersed interface method for elliptic equations with discontinuous coefficients and singular sources. *SIAM Journal on Numerical Analysis* 31:1019–1044.
<https://doi.org/10.1137/0731054>.
8. **Lee, L.** 2003. An immersed interface method for incompressible Navier-Stokes equations, *SIAM Journal on Scientific Computing* 25:832–856.
<https://doi.org/10.1137/S1064827502414060>.
9. **Li, Z.; Jaiman, R. K.; Khoo, B. C.** 2016. An immersed interface method for flow past circular cylinder in the vicinity of a plane moving wall, *International Journal for Numerical Methods in Fluids* 81:611-639.
<https://doi.org/10.1002/flid.4198>.
10. **Li, Z.; Lai, M. C.** 2001. The immersed interface method for the Navier-Stokes equations with singular forces *Journal of Computational Physics* 171:822–842.
<https://doi.org/10.1006/jcph.2001.6813>.
11. **Le, D. V.; Khoo, B. C.; Peraire, J.** 2006. An immersed interface method for viscous incompressible flows involving rigid and flexible boundaries, *Journal of Computational Physics* 220(1):109–138.
<https://doi.org/10.1016/j.jcp.2006.05.004>.
12. **Calhoun, D.** 2002. A Cartesian grid method for solving the two-dimensional streamfunction–vorticity equations in irregular regions, *Journal of Computational Physics* 176:231–275.
<https://doi.org/10.1006/jcph.2001.6970>.
13. **Ghafouri, A.; Esmaily, R.; Alizadeh, A.** 2018. Numerical simulation of tank-treading and tumbling motion of red blood cell in the poiseuille flow in a microchannel with and without obstacle, *Iranian Journal of Science and Technology, Transactions of Mechanical Engineering* 32:1-12.
<https://doi.org/10.1007/s40997-018-0233-2>.
14. **Abid Mattie, A.; Alizadeh, A.** 2019. Using a non-conforming meshes method to simulate an interaction between incompressible flow and rigid and elastic boundaries, *Mechanika*: 25 1-12.
<https://doi.org/10.5755/j01.mech.25.4.22975>.
15. **Russell, D.; Wang, Z. J.** 2003. A Cartesian grid method for modeling multiple moving objects in 2D incompressible viscous flow, *Journal of Computational Physics* 191:177–205.
[https://doi.org/10.1016/S0021-9991\(03\)00310-3](https://doi.org/10.1016/S0021-9991(03)00310-3).
16. **Xu, S.; Wang, Z. J.** 2008. A 3D immersed interface method for fluid–solid interaction, *Computer Methods in Applied Mechanics and Engineering* 197:2068–2086.
<https://doi.org/10.1016/j.cma.2007.06.012>.
17. **Brown, D. L.; Cortez, R.; Minion, M. L.** 2001. Accurate projection methods for the incompressible Navier–Stokes equations, *Journal of Computational Physics* 168:464–499.
<https://doi.org/10.1006/jcph.2001.6715>.
18. **Goldstein, D.; Handler, R.; Sirovich, L.** 1993. Modeling a no-slip flow with an external force field, *Journal of Computational Physics* 105:354-366.
<https://doi.org/10.1006/jcph.1993.1081>.
19. **LeVeque, R. J.; Li, Z.** 1997. Immersed interface method for Stokes flow with elastic boundaries or surface tension, *SIAM Journal on Scientific Computing* 18:709–735.
<https://doi.org/10.1137/S1064827595282532>.
20. **Ye, T.; Mittal, R.; Udaykumar, H. S.; Shyy, W.** 1999. An accurate Cartesian grid method for viscous incompressible flows with complex immersed boundary, *Journal of Computational Physics* 156:209-240.
<https://doi.org/10.1006/jcph.1999.6356>.
21. **Klekar, K. M.; Patankar, S. V.** 1992. Numerical prediction of vortex shedding behind square cylinders, *International Journal for Numerical Methods in Fluids* 14:327-341.
<https://doi.org/10.1002/flid.1650140306>.
22. **Okajima, A.** 1982. Strouhal numbers of rectangular cylinders, *Journal of Fluid Mechanics* 123:379-398.
<https://doi.org/10.1017/S0022112082003115>.
23. **Breuer, M.; Bernsdorf, J.; Zeiser, T.; Durst, F.** 2000. Accurate computations of laminar flow past a square cylinder, *International Journal of Heat and Fluid Flow* 21:186-196.
[https://doi.org/10.1016/S0142-727X\(99\)00081-8](https://doi.org/10.1016/S0142-727X(99)00081-8).

As'ad Alizadeh, Hussein Jebrail Zekri, S. Jafarmadar

NUMERICAL SIMULATION OF THE FORMATION OF VORTICES AROUND RIGID CYLINDERS AS AN ISSUE OF FLUID-STRUCTURE INTERACTION USING IMMERSED INTERFACE METHOD

S u m m a r y

The numerical simulation of the flow of fluid through one or a set of objects that causes the flow to separate from the surface of them has been the subject of interest by researchers over the past few decades. One of the most important types of these objects is those with a square cross section which have important and diverse applications in different industries. One of the practical applications of these types of streams is flow around chimneys, high-rise buildings, naval structures, suspended bridges, airplane wings, ship propellers and ducts. In this research, the immersed interface method is used which is a non-conforming method to the boundary. Eulerian mesh for fluid field, and Lagrangian mesh for solid field is used. The connection of these two networks is established by the Dirac Delta function. Considering the cylinder as a rigid immersion boundary within the flow. First, the flow around a square cylinder was simulated and we surveyed different flow patterns. The changes in the number of Strouhal and the Drag coefficient were investigated in different Reynolds. The flow around the two cylinders was simulated. It was observed that with the increase of Reynolds number and the gap between cylinders, the vortex shedding (Strouhal number) would increase.

Keywords: vortex shedding, rigid cylinder, drag coefficient, immersed interface method.

Received April 15, 2019

Accepted February 03, 2020